Probing f-Actin Flow by Tracking Shape Fluctuations of Radial Bundles in Lamellipodia of Motile Cells

G. Danuser*† and R. Oldenbourg†
*Department of Materials, ETH Zurich, Schlieren, Switzerland, and †Marine Biological Laboratory, Woods Hole, Massachusettes 02543 USA

ABSTRACT We examined the dynamics of radial actin bundles based on time-lapse movies of polarized light images of living neuronal growth cones. Using a highly sensitive computer vision algorithm for tracking, we analyzed the small shape fluctuations of radial actin bundles that otherwise remained stationary in their positions in the growth cone lamellipodium. Using the tracking software, we selected target points on radial bundles and measured both the local bundle orientations and the lateral displacements between consecutive movie frames. We found that the local orientation and the lateral displacement of a target point are correlated. The correlation can be explained using a simple geometric relationship between the lateral travel of tilted actin bundles and the retrograde flow of f-actin structures. Once this relationship has been established, we have turned the table and used the radial bundles as probes to measure the velocity field of f-actin flow. We have generated a detailed map of the complex retrograde flow pattern throughout the lamellipodium. Such two-dimensional flow maps will give new insights into the mechanisms responsible for f-actin-mediated cell motility and growth.

INTRODUCTION

When living cells are observed at high spatial resolution and in short time intervals, the motion of cell components is often dominated by seemingly random positional fluctuations. What looks like disturbing thermal noise at first sight is in fact a bearer of valuable information about the dynamic properties of the cell interior. In cell biological studies, fluctuation analysis was mainly applied to in vitro systems at the level of single molecules and molecular assemblies. For instance, fluctuation analysis has shed light on the mechanical properties of stiff, long, biopolymers, such as microtubules and actin filaments (Gittes et al., 1993), and on the molecular mechanisms of mechanoenzyme-substrate interactions such as myosin-actin (Ishijima et al., 1991), kinesin-microtubule (Gelles et al., 1988; Svoboda et al., 1993), and RNA polymerase-DNA (Yin et al., 1994). In each of these studies, the essential insight was gained from measuring and analyzing the positional dynamics of small objects, mainly markers in the form of beads, under the microscope.

A quantitative analysis of structural fluctuations inside living cells, however, has not yet been attempted. The main obstacle arising with in vivo studies is the complexity of the cell architecture. The use of distinct markers is often impossible and direct measurements on the target structures require sophisticated image analysis tools that are not supported by standard image processing packages.

In this paper we describe a framework using fluctuation analysis for observations inside a living cell. We continue a series of articles that report the study of the birefringent fine structure of growth cones located at the tip of growing *Aplysia* bag cell neurons. Using a new type of polarized light microscope (the "Pol-Scope," (Oldenbourg and Mei, 1995; Oldenbourg, 1996)), we recorded birefringence maps and assembled them into time-lapse movies that documented the creation and dynamic behavior of filopodia at the leading edge and of radial actin bundles in the lamellipodium of neuronal growth cones (Katoh et al., 1999b). By analyzing the time-lapse movies we found a close relationship between the behavior of filopodia and the arrangement of actin bundles in the whole lamellipodium (Katoh et al., 1999a). We further established that the lateral motion of tilted actin bundles and filopodia that move across the growth cone is the result of retrograde flow of actin filaments and their assembly near the leading edge of the lamellipodium (Oldenbourg et al., 2000). This conclusion was based on the experimental verification of a simple geometric relationship among the speed of lateral movement, speed of retrograde flow, and the tilt angle between the bundle axis and direction of retrograde flow. In the present paper we use the same geometric relationship to analyze the swaying motion of stable radial actin bundles in the lamellipodium.

The swaying motion of radial actin bundles in the neuronal growth cone is characterized by lateral displacements of the bundles and by small changes in their orientation (Fig. 1). We quantified the fluctuations in both position and orientation using a recently developed computer vision framework capable of measuring object displacements that are $<1/20$ of the classical resolution limit of the microscope (Danuser et al., 2000). No artificial markers were necessary to track the bundles inside the living cell. The tracker is designed to follow the position and orientation of an arbitrary linear structure and is optimized for the weak signal-

Received for publication 19 July 1999 and in final form 30 March 2000.
Address reprint requests to Dr. Gaudenz Danuser, Laboratory for Biomechanics, ETH Zurich, Wagistrasse 4, CH-8952 Schlieren, Switzerland. Tel.: 41-1-633-6214; Fax: 41-1-633-1124; E-mail: danuser@biomech.mat.ethz.ch.

0006-3495/00/07/191/11 $2.00

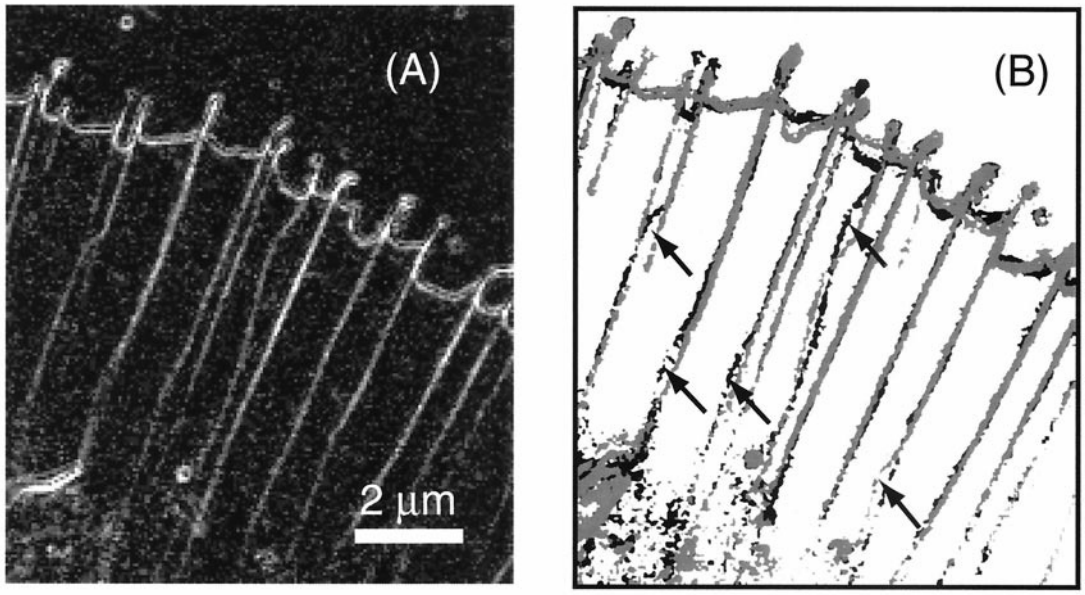

FIGURE 1 Positional fluctuations of radial actin bundles. (*A*) Birefringence image of a portion of the lamellipodium of a neuronal growth cone. The birefringence of radial actin bundles is due to the alignment of 10 to 40 actin filaments (Katoh et al., 1999b). The random meshwork of actin filaments located between the bundles is nearly isotropic and is, therefore, invisible in birefringence imaging. The existence of such a meshwork has been described in detail by structural studies using fluorescence labeling or electron microscopy. (*B*) Binarized birefringence signal and montage of a double exposure at two time points 50 s apart. Binarization is accomplished by thresholding the original signal. The black signal represents the thresholded birefringent structures at time point 1, the light gray signal those at time point 2. Notice that the bundle lengths, the positions of the associated filopodia, and the general axis orientations do not significantly change over this period. Yet, there are shape variations that cause local displacements of the bundles perpendicular to their axes. Arrows point to positions where the displacements are clearly recognizable.

to-noise ratio generally encountered in high-resolution, non-fluorescent light microscopy.

Our statistical analysis revealed that the lateral displacement and the orientation of a bundle are correlated with each other. The observed correlation can be explained on the basis of the same geometric model that was introduced in Oldenbourg et al. (2000) to explain the coupling between the lateral motion of tilted bundles and retrograde flow of f-actin-based structures. We show that the correlation can be used to estimate the direction and speed of retrograde flow at any location along a radial bundle. Therefore, the radial actin bundles can be considered probes for mapping out the direction and speed of the retrograde flow field throughout the lamellipodium.

This technique allowed us to determine the retrograde flow of filamentous actin with unprecedented resolution and precision. Rearward actin flow has been observed by many other researchers, mostly based on fluorescence microscopy (Small et al., 1999). To recognize the flow, fiduciary markers were introduced to highlight portions of the actin meshwork. For example, markers were generated by spot photobleaching (Wang, 1985), activation of caged fluorescence (Theriot and Mitchison, 1991) or in the form of membrane-bound beads that coupled to the intracellular actin meshwork (Lin and Forscher, 1995). The disadvantage of these techniques is the very sparse flow-field representation, which is obtained from tracking a few distinct markers. Also, the techniques do not locally probe the flow field. They rely on an evaluation of the marker movement along a trajectory of certain length. Spatial flow-field variation over distances shorter than the observed trajectory length are masked. The recently discovered technique of speckled fluorescent labeling of polymer assemblies can, in principle, remedy both drawbacks (Waterman et al., 1998). Yet, the complexity of the speckle signal has hitherto precluded a robust analysis of the flow-field dynamics.

Because of the high density of our flow-field representation and the truly local probing, we were able to analyze the retrograde flow in more detail. We divided the measured flow field into two superimposed movement components: a centripedal flow perpendicular to the mean hemispherical shape of the leading edge, and a second field exhibiting local variations in flow velocity. The speed of the first field was assumed to be constant throughout the lamellipodium, while the velocity of the second field could vary in direction and speed. We conclude that there is significant transport of f-actin along trajectories that deviate from the global poleward flow direction. Also, the speed of retrograde flow appears to vary significantly over the whole lamellipodium. This finding gives an entirely new view of the properties of actin flow. The biomechanical interpretation of this result will be subject of future research, while the present paper

focuses on fluctuation analysis as the key to probing the meshwork dynamics.

MATERIALS AND METHODS

The materials and methods regarding the *Aplysia* bag cell cultures and the imaging of individual growth cones using a new type of polarized light microscope are described in Oldenbourg et al. (2000) and in a previous article (Katoh et al., 1999b).

Fluctuation analysis with computer vision

We have analyzed the swaying motion of radial actin bundles using an in-house developed tracking package (the package builds on MATLAB 5.2, Mathworks Inc., as a basis and integrates C routines for computationally expensive tasks) (Danuser et al., 2000). The tracker achieves the sub-pixel sensitivity that is required for the analysis of the minute fluctuations in bundle position and orientation. It measures simultaneously positional and orientational variations in any target point along the bundle. The average precision in shift and rotation measurements, and thus the minimum displacement and orientation change that are significantly quantifiable, amounts to 0.09 pixel in image space and 0.5°, respectively. These values were obtained by converting the signal-to-noise ratio of bundle images into a geometric tracking uncertainty. In the analyzed Pol-Scope images 1 pixel corresponds to 115 nm in object space. Thus, the minimal displacement of a bundle discernible with the tracker measures ~10 nm.

Fig. 2 depicts the essential parameters involved in the tracking of bundle fluctuations. All the geometric developments are made in a left-handed coordinate system, as customary in image processing. Consider a target point on a radial actin bundle. The target point coordinates at time t are given by the vector $\mathbf{x}(t)$. The local orientation of the bundle axis at this position and time point is represented by the angle $\phi(t)$ between the horizontal image axis and the direction tangential to the bundle. One time step later the target point is localized at $\mathbf{x}(t + 1)$. The stretch between the locations $\mathbf{x}(t)$ and $\mathbf{x}(t + 1)$ is locally perpendicular to the bundle axis at time t. Therefore, we term it the lateral displacement $\delta_{\text{lateral}} = |\mathbf{x}(t + 1) - \mathbf{x}(t)|$. We constrain the tracking to displacements perpendicular to the axis because the motion component parallel to the axis is not observable unless the target point is represented by a fiduciary marker. Over the same time period the orientation of the bundle axis change by $d\phi = \phi(t + 1) - \phi(t)$.

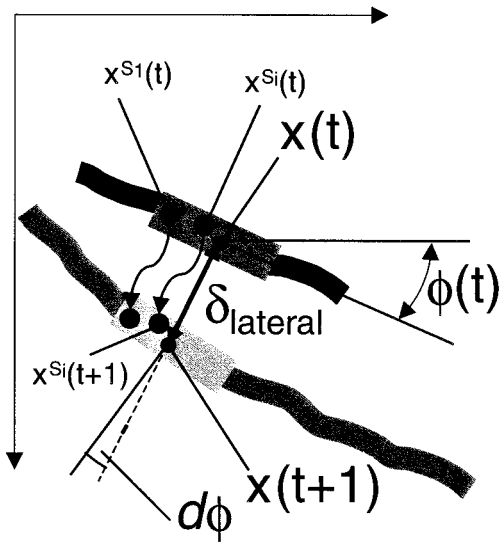

FIGURE 2 Principle of tracking the lateral movement of a bundle segment. Given a target point on the bundle at time t, its new location at time $t + 1$ is defined as the intersection between the bundle in its new position and the normal to the bundle in the target point at time t. For each member S_i of the sample set Ω, which forms the image of the bundle segment around the target point, a correspondent is searched in the frame captured one time step later. The search is constrained by parametric models describing the geometric and photometric inter-frame variability of the segment image. Geometric parameters that describe the motion of the tracked segment include 1) the displacement δ_{lateral} along the normal and 2) the change in segment orientation $d\phi = \phi(t + 1) - \phi(t)$. Cf. text for further parameters.

Also in Fig. 2 the principle of tracking is sketched. Consider a set of N samples $\Omega = \{S_1, \ldots, S_i \ldots, S_N\}$ which forms the image of the tracked bundle segment around the target point. Tracking a whole segment is necessary because the orientation of a line image cannot be measured truly locally. The length of the segment must be kept short such that bending only minimally affects the measurement. At time t the sample S_i is located at $\mathbf{x}^{S_i}(t)$ and takes a brightness value $I^{S_i}(t)$. As the segment image moves, one time step later the sample is located at $\mathbf{x}^{S_i}(t + 1)$ and takes a brightness value $I^{S_i}(t + 1)$. The brightness variations mainly originate from changes in bundle composition (Oldenbourg et al., 1998) and from bundle movements in Z-direction. Both positional and brightness variations of the sample are described by parametric models:

$$\mathbf{x}^{S_i}(t) \rightarrow \mathbf{x}^{S_i}(t + 1) : \mathbf{x}^{S_i}(t + 1) = \mathbf{g}(\mathbf{x}^{S_i}(t), \xi^G) \quad (1)$$

$$I^{S_i}(t) \rightarrow I^{S_i}(t + 1) : dI^{S_i} = I^{S_i}(t + 1) - I^{S_i}(t) = f(I^{S_i}(t), \xi^P) \quad (2)$$

Equation 1 describes the transformation of the sample coordinates as a function $\mathbf{g}(\mathbf{x}^{S_i}(t), \xi^G)$ subject to a *geometric* parameter vector ξ^G. The parameter vector includes the above-mentioned lateral displacement δ_{lateral} and rotation $d\phi$. In addition, we need to take into account that the bundle can fluctuate in Z-direction. This causes blur variations in the bundle image that are modeled with a linear scaling parameter μ. Equation 2 denotes the change in sample brightness $I^{S_i}(t)$ as a function $f(I^{S_i}(t), \xi^P)$ subject to the brightness $I^{S_i}(t)$ itself and a vector ξ^P of *photometric* parameters. It consists of two parameters, one for contrast and one for additive brightness changes.

We assume that the coordinate transformation of the target point obeys the same parametric model as the transformations of the surrounding image samples, thus

$$\mathbf{x}(t) \rightarrow \mathbf{x}(t + 1) : \mathbf{x}(t + 1) = \mathbf{g}(\mathbf{x}(t), \xi^G).$$

Consequently, target point tracking essentially means finding an estimate for the geometric transformation parameters ξ^G, which then allows us to map the coordinates $\mathbf{x}(t)$ into $\mathbf{x}(t + 1)$. The parameter estimation is accomplished by best matching the two images of the segment at the time points t and $t + 1$. The matching strategy and the technical details for computing the solution are discussed in depth in Danuser et al. (2000).

The initialization of the tracker, i.e., the definition of $\mathbf{x}(0)$ and $\phi(0)$, is also supported by computer vision algorithms. The operator interactively draws a box close to the target point to be analyzed. After manual box initialization a line extraction algorithm automatically localizes the bundle axis, defines the target point as the axis point closest to the center of the box, and determines the local orientation of the bundle segment in this point. The length of the segment is defined by the perimeter of the manually set box. The positional and orientational precision of the line extractor amounts to ~0.2 pixels, respectively 1°.

Another important task of initialization is the selection of the sample set Ω, which actually forms the image of the bundle segment enclosing the target point. This task is accomplished in the same step as line extraction. As a byproduct of the line extractor an estimate of the local line width is available for each point on the bundle axis. This information enables the

selection of all samples belonging to the image of the tracked bundle segment. The selection of Ω needs to be executed with particular care. If the set is too narrow in width, i.e., samples at the periphery of the segment image are omitted, the tracking result will get more susceptible to noise. If the set is too wide, i.e., samples are included that do not belong to the segment image but to the surrounding background, two types of errors will deteriorate the tracking. 1) Both inter-frame variability models Eqs. 1 and 2 are strictly formulated for samples belonging to the image of a bundle segment. Background pixels obey different transition rules. Including such pixels in the computation will distort the estimation of the tracking parameters. 2) If the sample set exceeds the segment image in width it may interfere with the image of another, e.g., laterally traveling bundle coming close in the course of the movie. Interfering samples will deteriorate the parameter estimation in the same way as superfluous samples from the background.

Fig. 3 *A* displays the outcome of a segment initialization. The operator drew a box of the same size as the yellow box somewhere near the bundle. Segment axis, target point position (*green dot*), local orientation (*green line perpendicular to the bundle*), and the sample set (*magenta*) forming the image of the segment were then computed based on automatic line extraction. The yellow box overlaid to the display is centered on the target point and serves the visualization of the tracking result. Fig. 3 *B* shows the same image portion 25 frames later. Over this period, the bundle has laterally moved 2.06 pixels (barely noticeable by eye) and rotated 3.4°. The rotation is visualized by the yellow box. It is constructed by applying the estimate for the coordinate transition $\mathbf{x}(t) \rightarrow \mathbf{x}(t+1)$ to the four corners of the yellow box in Fig. 3 *A*. Also, notice the subtle scaling ($\mu = 0.92$) between the segment images. The scaling is reflected by a decrease of the box area from Fig. 3 *A* to 3 *B*.

RESULTS

We investigated the swaying motion of radial actin bundles in the growth cone of an *Aplysia* bag cell neuron that was imaged in a time-lapse movie recorded with the Pol-Scope (Movie 1 in Katoh et al., 1999b). We selected target points on radial actin bundles in the lamellipodium and followed their position and the orientation of the bundle segments using the tracking package described in the Materials and Methods section.

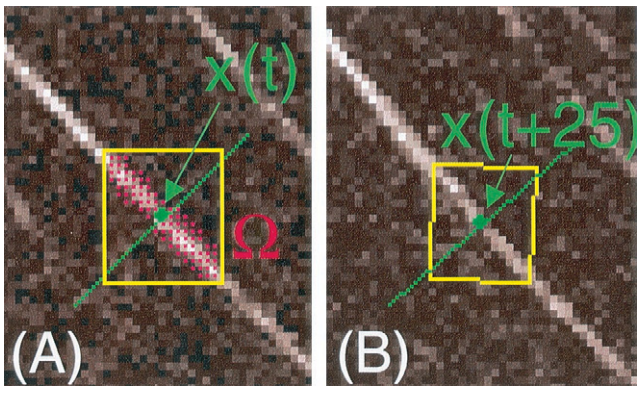

FIGURE 3 Initialization and tracking of a bundle segment. (*A*) Initialization of the target point and sample set in the first frame of the movie. The green dot indicates the position of the target point centered on the bundle axis. The green line depicts the direction perpendicular to the bundle axis. Samples belonging to the data set selected for tracking are colored magenta. (*B*) Result from tracking the target point and surrounding segment image over 25 frames. The movement relative to the image in (*A*) is barely visible. The orientation and size of the yellow box indicates that the segment image has also been rotated and scaled.

The graph in Fig. 4 *A* displays the results from tracking a target point over a time span of 15 min sampled at 5 s between frames. The graph shows the measured lateral displacement δ_{lateral} of the target point between consecutive frames of the time-lapse movie versus the local orientation ϕ of the bundle axis. The diagonal distribution of 183 data pairs indicates that there exists a correlation between bundle orientation and lateral displacement. The correlation coefficient is 57.1%. For comparison, the average correlation coefficient between 183 number pairs distributed randomly over the same value range amounts to 0.5% (average of 50 numerical experiments). We analyzed the correlation by linear regression using robust statistics (Danuser and Stricker, 1998). Three data outliers were detected by the regression algorithm and eliminated from fitting (labeled with square markers). The relatively wide spread of the data cluster around the regression line in Fig. 4 *A* originates in the fact that both displacement and orientation measurements are at the resolution limit of the computer vision tracker. As mentioned in the Materials and Methods section, the signal-to-noise ratio of the Pol-Scope permits a tracking precision of 0.09 pixels (10.4 nm) in displacement and 0.5° in orientation. The bulk part of the displacements analyzed in Fig. 4 *A* is below 0.4 pixel, thus the relative measurement error of most of the data points is >25%.

We have analyzed the dependence of the correlation coefficient on the step size of the displacement. In first approximation, the tracking precision is independent of the step size and rotation performed by the bundle segment. Thus, the relative error of the data points will decrease with a larger displacement step. On average, the displacement step increases with the elapsed time between two frames. Fig. 4 *B* displays the relationship between lateral displacements and bundle orientations for the same segment as in Fig. 4 *A,* however, with a fourfold longer period between the time points. Instead of tracking the bundle segment between consecutive frames of the movie (frame rate 5 s), we let four frames pass and measure the displacement and rotation over 20 s. To generate as many data points as possible, we tracked each segment four times through the 15-min movie sequence, in the first run over the frames 1, 5, 9, . . . , in the second run over the frames 2, 6, 10, . . . , etc. Indeed, with the larger mean lateral displacement, the correlation improves from 57.1% to 92.0%.

Yet, there are two limits to this procedure of noise suppression: 1) the longer the interval between the considered time points, the higher the probability that the segment does not move monotonically in one direction but passes a turning-point in the oscillating trajectory. In this situation the value of lateral displacement will be nonsensical. 2) As shown in the Discussion, our simple fluctuation tracking suffers a systematic error, which is negligible only for small

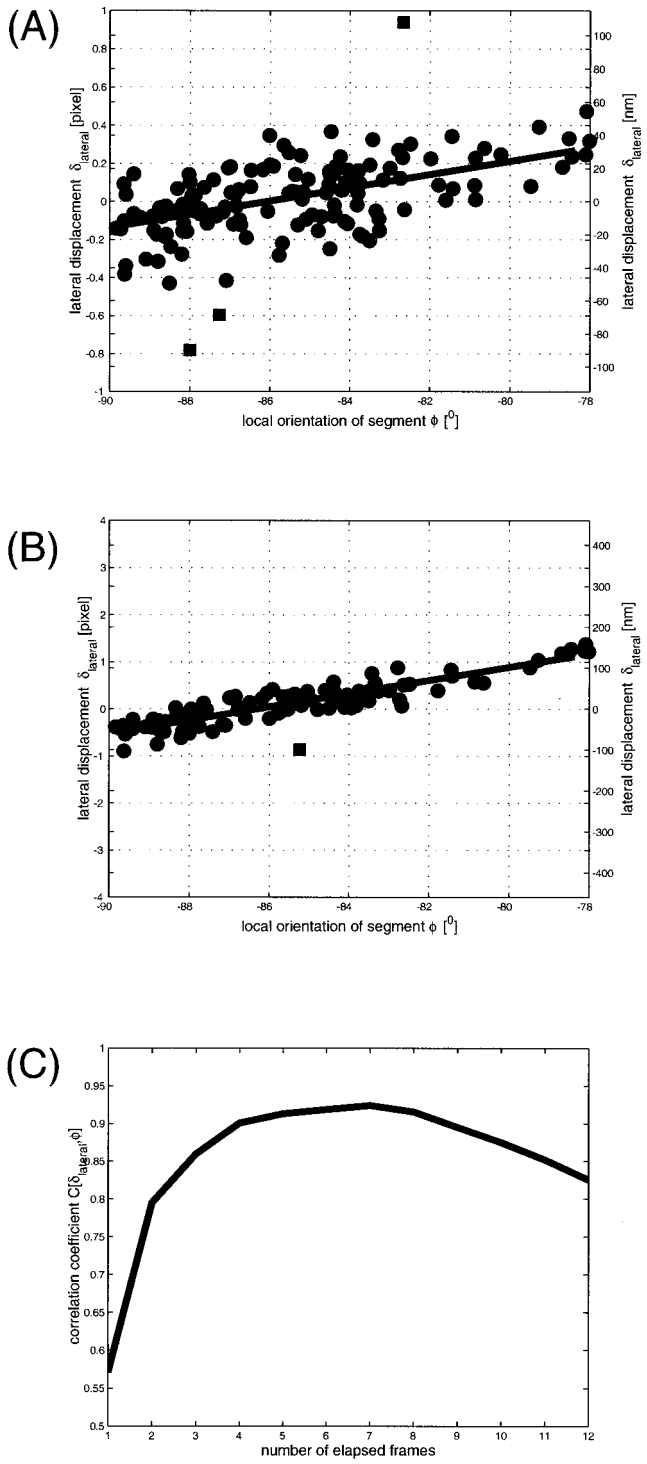

FIGURE 4 Results of tracking the swaying motion of a radial actin bundle. The lateral displacements of a target point on the bundle versus bundle orientations are measured with subpixel resolution. (*A*) Displacement-orientation data distribution obtained from tracking a target point between consecutive frames of a 15-min movie sampled at 5-s time intervals. (*B*) Distribution obtained from the same image data, but tracking the target point over intervals of 20 s, i.e., in steps of four frames. The reduced data scatter indicates that larger time steps can reduce the relative tracking error. However, there are limits to this way of noise reduction, which are explained in detail in the text. (*C*) Correlation coefficient between lateral displacement and bundle orientation as a function of elapsed frames. The data correlation is highest for four to eight elapsed frames, i.e., 20–40-s time intervals between the data points. For time intervals shorter than 20 s (less than four frames) random tracking errors deteriorate the correlation coefficient. For time intervals beyond 40 s (more than eight elapsed frames) systematic errors are introduced into the fluctuation analysis that decrease the correlation coefficient. In (*A*) and (*B*) the diagonal distribution of data points reflects the correlation between bundle orientation and lateral displacement. The correlation is characterized by a regression line that is overlaid to the data points. As discussed in the text, the slope of the line is a direct measure of the speed of retrograde flow of f-actin structures in the lamellipodium and the zero crossing indicates the direction of retrograde flow in the vicinity of the target point. Line fitting is performed in conjunction with robust statistics to automatically eliminate outlier data (Danuser and Stricker, 1998). Inlier data are labeled with dots, outlier data with squares. On a 99% confidence level three and one outliers are detected for the data sets in (*A*) and (*B*), respectively.

segment rotations. With a larger time interval between the processed frames the average segment rotation will increase. The data points will be perturbed by this rotation-related error to an extent that precludes linear regression analysis. Both arguments are confirmed by the graph in Fig. 4 *C,* which displays the correlation coefficient as a function of the number of elapsed frames. The correlation coefficient reaches a maximum between four and eight elapsed frames, i.e., 20–40-s intervals between data points. We conclude that for intervals longer than 20 s the positive impact of reduced relative measurement errors is outweighed by the aforementioned systematic effects. Beyond 40-s intervals the latter begin to dominate random tracking errors and deteriorate the correlation. For other bundle segments we have observed maximum correlation coefficients between three and six rather than four and eight elapsed frames. Thus, we chose four elapsed frames as the optimum time step to pursue the final regression analysis, as described in the following.

The regression line is characterized by two parameters, the zero crossing ϕ_0 and the slope $\Delta\delta/\Delta\phi$. The zero crossing is the orientation for which zero lateral displacement is measured. The linear relationship between displacement and orientation of the bundle in the target point can be expressed by the equation:

$$\delta_{\text{lateral}} = \frac{\Delta\delta}{\Delta\phi}(\phi - \phi_0). \tag{3}$$

For the physical interpretation of slope and zero crossing we turn to the model introduced in Oldenbourg et al. (2000) that relates the lateral motion of tilted bundles to the observed retrograde flow of fiduciary structures in the f-actin meshwork. Using this model we postulate that also the positional fluctuations of stationary bundles originate from retrograde flow in the actin meshwork. The fluctuations are caused by variations in the orientation of consecutive bundle segments. The orientation of a segment is determined during

polymerization at the leading edge. Similar to fiduciary structures, the orientation of a bundle is preserved in the meshwork during its retrograde travel through the lamellipodium. Focusing on a target point located on a radial bundle at a fixed distance behind the leading edge, bundle parts pass that have been polymerized at different times. Temporal variations in segment orientation manifest themselves as rotational fluctuations of the local bundle axis in the observed point. Also, they cause small displacements of the bundle axis that are recognized as a swaying motion. Typically, we have to wait for a few frames to pass until the changes in axis geometry become appreciable by eye. However, the computer vision tracker is sensitive enough to resolve the fluctuations on a frame-to-frame basis.

In the paper by Oldenbourg et al. (2000) we found that stationary, radial actin bundles, on average, are oriented parallel to retrograde flow. Furthermore, when a bundle is tilted with respect to the direction of retrograde flow, the bundle exhibits lateral motion whose speed increases with the tilt angle. We found that the following relationship holds between the tilt angle α, the speed of retrograde flow v_{retro}, and the speed of lateral motion $v_{lateral}$:

$$v_{lateral} = v_{retro} \sin \alpha. \quad (4)$$

Fig. 5 illustrates the geometric relationship between the variables in Eq. 4. in the context of the swaying motions of radial actin bundles.

Equations 3 and 4 are indeed very similar after introducing the following substitutions. First, we can interpret ϕ_0 as the direction of retrograde flow, i.e., $\alpha = \phi - \phi_0$. Second, since in a stationary bundle the difference between bundle orientation and zero crossing is smaller than 10°, we can replace the sine function by the linear term of its polynomial expansion, $\sin(\phi - \phi_0) \approx (\phi - \phi_0)$. Finally, we interpret the lateral displacements per time interval Δt between two frames as the speed of lateral motion, i.e., $\delta_{lateral}/\Delta t = v_{lateral}$. Introducing these substitutions in Eqs. 3 and 4 and comparing their terms, we find

$$v_{retro} = \frac{\Delta\delta}{\Delta\phi} \cdot \frac{1}{\Delta t}.$$

It turns out that the slope of the regression line divided by the time interval Δt yields the speed of retrograde flow. Fluctuations in position and orientation of radial actin bundles therefore give us a means to measure the speed and direction of retrograde flow in the observed target point.

The line fit through the data pairs in Fig. 4 *B* yields $\phi_0 = 93.68 \pm 0.14°$ for the zero crossing and $v_{retro} = 2.78 \pm 0.13$ μm/min. The standard deviations of the line parameters were propagated from the spread in the data pair distribution. Interestingly, the above regression parameters do not differ statistically from a line fit to the data in Fig. 4 *A*: $\phi_0 = 93.92 \pm 0.37°$ and $v_{retro} = 2.76 \pm 0.34$ μm/min. Obviously, longer time intervals result in higher data correlation and thus higher fitting precision, but do not change the regression parameters. The data points in Fig. 4 *A,* which have much larger relative error, scatter around the same regression line as those in Fig. 4 *B.* From this we conclude that the tracking errors causing the data scatter in Fig. 4 *A* are truly random, with zero mean. When using a sufficiently large set of input data points for regression analysis, the result becomes independent of the chosen time interval for tracking.

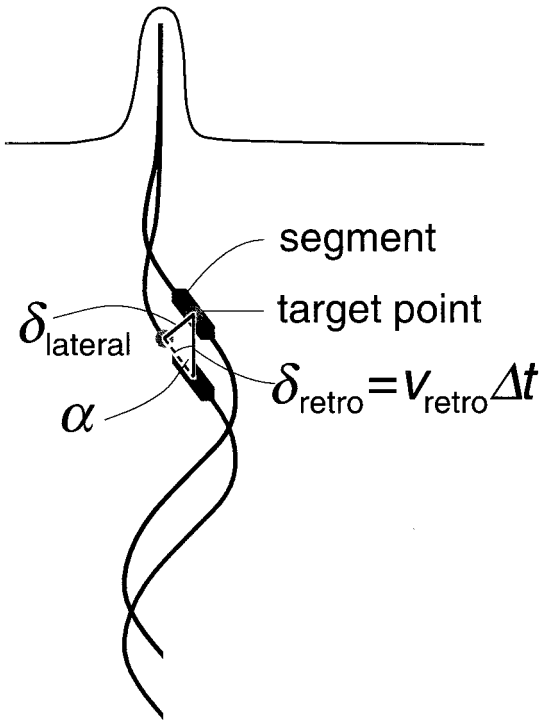

FIGURE 5 Schematic of filopodium with undulated radial actin bundle that participates in retrograde flow. Two positions of the bundle at two time points are drawn. The bundle is moving straight down by a distance $\delta_{retro} = v_{retro}\,\Delta t$, with Δt being the elapsed time. The bundle is translated only and no change in bundle shape is assumed. Bundle segments that are tilted by an angle α with respect to retrograde flow seem to move laterally by a distance $\delta_{lateral}$. The lateral movement is measured by tracking a target point on the bundle as described in Materials and Methods. Note that the physical bundle segment moves straight down, while the target point moves laterally.

A further investigation of the regression properties in Appendix A indicates that the parameters are also independent of the bundle undulation and thus of the persistence length of the actin bundle.

We performed the fluctuation analysis for multiple segments of radial bundles distributed over the entire lamellipodium. Bundles whose image signal appeared or disappeared during the movie sequence were not considered. Fig. 6 gives a graphic overview of the measurements. The retrograde flow vectors are overlaid in red to the first frame of the Pol-Scope movie. Notice that not all target points come to rest on a bundle in this image. We take the centers

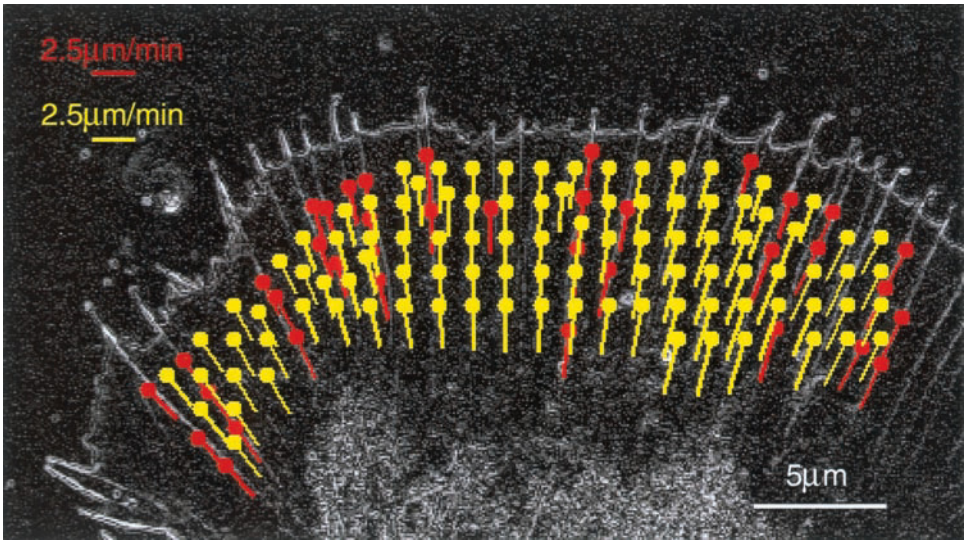

FIGURE 6 Vectorial representation of the flow field overlaid to the first image of the Pol-Scope movie. The red vectors show points where the retrograde flow was actually measured by fluctuation analysis. The yellow vectors were interpolated from the measurements to generate a more continuous flow map. A remarkable property of the field is the acceleration of flow from the left to the right side of the lamellipodium.

of the fluctuation trajectories as the origins for plotting the vectors. The centers define the mean locations of the target points on a radial bundle. Some of the centers have an offset relative to the image of the bundle. This gap reflects the deviation of the bundle in the first frame from the mean target position.

Pooling all the target points across the lamellipodium, the average speed of retrograde flow over all points amounts to 2.37 ± 0.13 μm/min. The standard deviation of a single speed measurement is 0.71 μm/min. This value clearly contrasts with the average precision of a speed estimate of 0.22 μm/min propagated from the data scatter in line regression. We conclude that the much higher standard deviation obtained from data pooling originates from a significant spatial variation of retrograde flow across the lamellipodium. Indeed, this is appreciable in Fig. 6. The speed tends to increase from the left to right side of the lamellipodium. This becomes even more visible through the (yellow) overlay of interpolated retrograde vectors, which results in a dense representation of the retrograde flow field over a large sector of the growth cone. We investigate this behavior of retrograde flow in the Discussion section along with a further analysis of the performance and potential of our fluctuation method.

DISCUSSION

The average retrograde flow speed of 2.37 ± 0.13 μm/min estimated via fluctuation analysis is close to the value of 2.6 ± 0.25 μm/min measured directly by tracking structural features in the lamellipodium (Oldenbourg et al., 2000). Considering the standard deviations, the statistical significance of the difference is weak.

The agreement between the results supports the hypothesis that all recognizable dynamics of filopodia and actin bundles in the lamellipodium of the neuronal growth cone, including the swaying motion of radial bundles, can be fully explained within the framework of actin polymerization near the leading edge and of retrograde flow of the actin network. In addition, we postulate a mechanism that introduces orientational variation into bundle segments that are assembled near the leading edge. Once established at the leading edge, the orientation of a segment appears to be preserved during the retrograde transport through the lamellipodium. Although there are good reasons to speculate that the origin of these fluctuations is thermodynamic (Mogilner and Oster, 1996), the exact mechanism of bundle generation and the variations in orientation remain enigmatic (see Discussion in Oldenbourg et al., 2000).

Once the relationship between bundle fluctuations and retrograde flow is established, we can turn the table and suggest that the fluctuation of radial bundles can be used to study f-actin flow. Radial bundles can be regarded as *probes* that reveal the speed and direction of retrograde flow in which the bundles themselves participate. The idea of probing the flow field via fluctuation analysis of naturally formed, unstained bundles bears not only methodological beauty but yields novel possibilities to get insights into mechanisms of actin-based cell motility.

In neuronal growth cones and lamellipodia of other motile cells, radial bundles can be numerous and therefore can provide a dense array of probes for measuring the speed and direction of retrograde flow. Using the fluctuation analysis we can quantify the flow parameters in small regions around each chosen target point. Hence, the flow field can be mapped at high spatial resolution.

The temporal resolution of the fluctuation analysis is inversely proportional to the tracking errors. Given the random errors of the computer vision tracker, the temporal resolution is determined by the minimal number of displacement-orientation data pairs that are necessary for robust regression analysis. The shorter the time period the fewer

data pairs are available, thus the larger the standard deviation of the regression parameters. In the current study, the final regression parameters defining retrograde velocity in one target point were extracted from fluctuation data collected over a 15-min observation period. We could increase the time resolution by splitting the movie into multiple frame sequences of shorter observation periods, however, at the cost of decreased precision in the measured flow parameters.

Apart from the random tracking errors that average out with a sufficiently long observation period there is a systematic measurement error that causes the distribution of the displacement-orientation data pairs to deviate from a straight line in the $\{\delta_{lateral}, \phi\}$-domain. The geometric model shown in Fig. 5 is strictly correct only if the bundle curvature around the target point is zero. As illustrated in Fig. 7, for curved bundles the observed lateral displacement is not equal to the projection of retrograde displacement onto the normal of the bundle segment, but differs from it by a term ε. This term results in a systematic deviation of the measured data from the postulated model as written in Eqs. 3 and 4. For general bundle shapes Eq. 3 becomes

$$\delta_{lateral} + \varepsilon = \frac{\Delta\delta}{\Delta\phi}(\phi - \phi_0) \tag{5}$$

with ε depending on the local curvature. If we assume that a segment does not change the curvature during rearward movement we find that ε depends on the bundle rotation $d\phi$, the bundle tilt $\alpha = (\phi - \phi_0)$, and the retrograde displacement of the segment between two consecutive frames denoted by δ_{retro}:

$$\varepsilon \approx \delta_{retro}\cos\alpha \, d\phi \tag{6}$$

The orientational fluctuation $d\phi$ between two images of the segment is proportional to the bundle curvature in the target point. The shorter the intervals between two frames, the smaller is $d\phi$. In the limit $d\phi = 0$ there is no systematic deviation of the $\{\delta_{lateral}, \phi\}$ measurement distribution from a straight line.

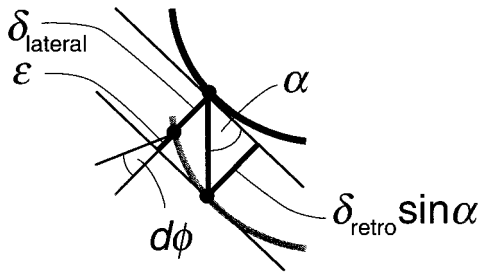

FIGURE 7 Systematic bias in the observed lateral displacement caused by bundle curvature. In the illustrated case of concave curvature, the lateral displacement $\delta_{lateral}$ measured between two target points is shortened by ε compared to the expected projection of retrograde displacement $\delta_{retro}\sin\alpha$. In the case of convex curvature, the displacement would be extended (not shown). The change in bundle orientation $d\phi$ between the two target points is related to the curvature of the bundle. Thus, the bias ε depends on the orientational fluctuation $d\phi$ between the frames and vanishes for $d\phi = 0$.

As mentioned in the Results section, this systematic error term was one of the two limits that precluded us of using tracking intervals of more than five to six elapsed frames, i.e., 25 s to 30 s (see Fig. 4 *C*). With larger intervals both δ_{retro} and $d\phi$ increase, which causes ε to increase nonlinearly with the tracking interval. For the data set shown in Fig. 4 *A* the mean systematic error $\bar{\varepsilon}$ over all data points amounted to 3.1 nm, while the maximum error ε_{max} was 13.5 nm. Compared to the random tracking error of 10 nm, the systematic error term appears to be negligible. Increasing the tracking interval to four elapsed frames in Fig. 4 *B*, the mean and maximum systematic errors amounted to $\bar{\varepsilon} =$ 24.8 nm and $\varepsilon_{max} = 116.7$ nm, respectively. Thus, comparing it again to the random tracking error of 10 nm the scatter of the data points in Fig. 4 *B* is, in contrast to Fig. 4 *A*, largely associated with the effect of bundle curvature. However, the statistical distribution of ε has a zero mean, since the average curvature of a radial bundle is zero. Therefore, analogous to the averaging of random tracking errors, the systematic measurement error cancels out in the regression analysis over a long enough observation period. We found that after 15 minute the systematic error distributes symmetrically around the regression line.

A fundamental strength of the fluctuation method consists in the truly local measurement of the flow field. In conjunction with dense sampling due to the large number of radial bundles spatial variations in retrograde flow can be detected. To explore this behavior we have implemented a statistic framework called *least-squares collocation* (LSC), which is capable of decomposing the retrograde flow field into a global flow trend described by a parametric model and a superimposed stochastic flow field with regional correlation. Additionally, the framework has filtering and interpolation capabilities, i.e., random errors are removed from the original velocity measurements and retrograde flow velocity vectors can be predicted at any location across the lamellipodium (for details see Appendix B).

Fig. 8 displays the result of our flow field decomposition by LSC. Panel (*A*) shows the filtered velocity vectors in all target points in red and the interpolated velocity vectors in yellow. Although barely appreciable by eye, the difference between the vectors in this panel and those in Fig. 6 is that here random errors in the velocity measurements (red vectors) have been removed. Panel (*B*) shows the trend function in both target and interpolation points. We have adopted a centripedal flow with constant speed as the global parametric function. This choice was motivated by the hemispherical shape of the growth cone. We assumed that the main direction of rearward f-actin movement would be perpendicular to the mean shape of the front edge of the protruding lamellipodium (dashed line overlay). Both center and speed of the global poleward flow were estimated as parameters in LSC. The location of the center falls outside the lamellipo-

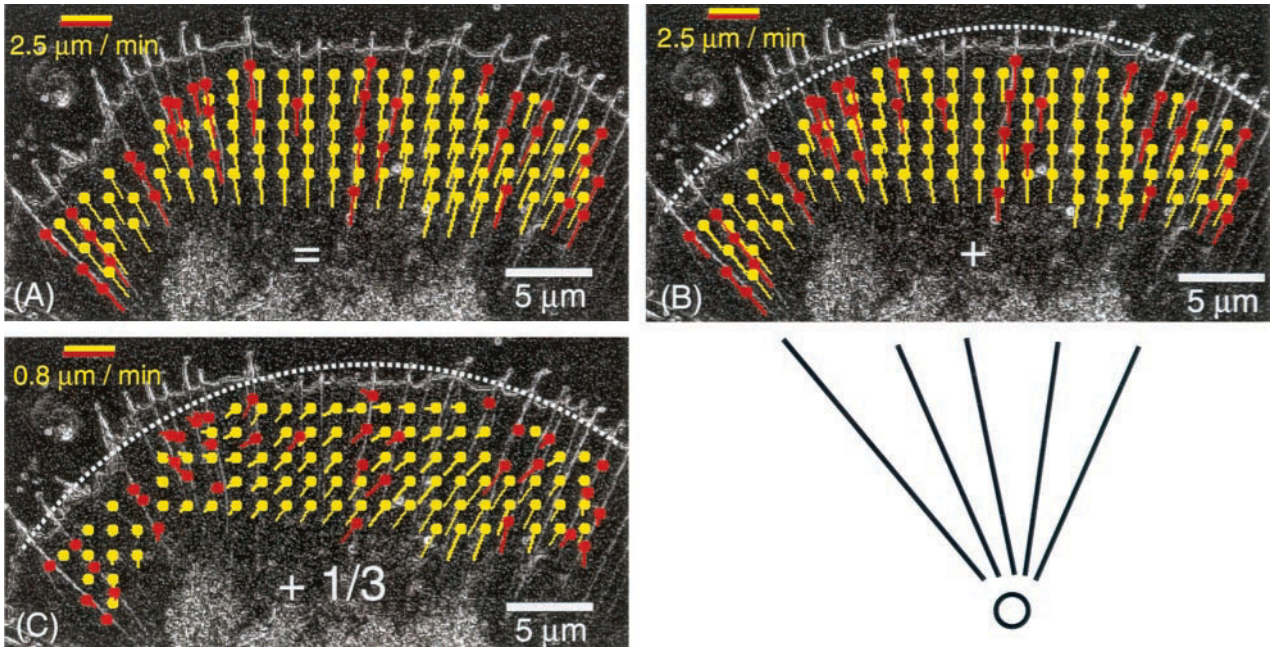

FIGURE 8 Flow field decomposition by LSC. (*A*) The filtered (*red*) and interpolated (*yellow*) velocity vectors. They are decomposed into a global centripedal flow with constant speed (*B*) and a stochastic flow field (*C*) with regionally correlated components. The latter is referred to as a disturbance field. The center of the global poleward flow is sketched underneath (*B*). Notice that the velocity vectors in (*C*) are enlarged three times for better visibility. Overlaid to (*B*) and (*C*) are dashed lines that represent the hemispherical mean shape of the leading edge. The center of the hemisphere is equal to the center of the poleward flow, i.e., the supposed global flow model as shown in (*B*) is always normal to the hemisphere. From qualitative analysis we speculate that there is a relationship between the superimposed stochastic flow field in (*C*) and the deviations of the actual leading edge from the hemisphere (see text for more details). A rigorous verification of this hypothesis will be the subject of future research.

dium and is sketched underneath panel (*B*). The speed was estimated to be 2.43 μm/min. Panel (*C*) displays the additional flow component in the target and interpolation points. We refer to this second component as a disturbance field to the global flow in panel (*B*). By vector addition the movements in panel (*B*) and (*C*) sum up to those in panel (*A*). Notice that for graphical purposes the vectors of the disturbance field are enlarged three times. The mean magnitude of the disturbance vectors amounts to 0.5 μm/min. The maximum vector is 1.1 μm/min long. In comparison, the mean random error that is filtered away from the measured velocity vectors is 0.2 μm/min. This means that the disturbance vectors are on average significantly larger than the error of a velocity measurement in a target point.

Fig. 8 gives a much more detailed view of retrograde flow in a lamellipodium than was previously available. While centripedal flow, which has been described before by other authors, is clearly dominant, there are statistically significant flow components that deviate from this pattern. This finding has been made possible by the density and high accuracy of the fluctuation-based velocity measurements. This complex flow behavior would not be visible by tracking a single structural feature as the general backward movement dominates the flow.

In the future, we anticipate the calculation of strains and stresses associated with the different flow types in the lamellipodium. Such analysis will fuse our dynamic observations with the largely known structural and elastic behavior of the actin meshwork. Also, now that we have the analysis tools at hand, we will investigate the correlation between the disturbance flow pattern and geometric deviations of the leading edge from the supposed mean shape model, in our case the hemisphere. Qualitatively, there appears to be a relationship between them (see Fig. 8 *C*). For instance, in the center section of the lamellipodium there is a sideways movement component in the disturbance field, which correlates with a flattened front of the leading edge. However, in the left section the disturbance flow tends to point in the forward direction. This phenomenon seems to be correlated with a faster advance of the leading edge in that section. Such comparison will be particularly interesting with fast protruding lamellipodia. There, temporal changes in membrane shape that are associated with cell growth or retraction will be compared with the temporal development of the disturbance flow pattern and modulations of the polymerization mechanisms that advance the leading edge.

To conclude, this paper proposes a new framework for the local measurement of retrograde flow in the lamellipodium of motile cells. We have exploited the minute shape fluctuations that are present in otherwise stable radial actin bundles. Our method allows us to generate a dense flow field representation that reveals subtle regional variations in flow direction and speed.

APPENDIX A

The regression analysis is independent of the bundle shape

Our proof goes along the following lines: if two bundles of sinusoidal shape with identical flow speed and direction but with different amplitude and wavelength generate identical regression lines in the data domain $\{\delta_{lateral}, \phi\}$, any arbitrary shaped bundle moving with this speed and direction will produce the same regression line. This statement holds because the shape of any bundle can be decomposed into a series of sinusoidal base functions with different wavelengths and amplitudes. Fig. 9 *A* depicts the retrograde movement of a bundle with a sinusoidal shape. It displays two time points of a bundle that moves from the left to the right along the horizontal axis. The bundle undulates according to a sine function with amplitude a and wavelength λ, thus $y_1 = a \sin(2\pi x/\lambda)$. The displacement of the bundle associated with a flow along x is accomplished by introducing a shift δ_{retro}, thus $y_2 = a \sin(2\pi (x - \delta_{retro})/\lambda)$. Also, in Fig 9 *A* we indicate the construction of the theoretical lateral displacement in any target point along the bundle. Analogous to the tracking procedure demonstrated in Fig. 2, the lateral displacement $\delta_{lateral}$ is determined by the distance between the target point and the intersection of the normal with the shifted bundle. The normal is calculated based on the orientation ϕ of the bundle tangent in the target point. Notice that in the setting of Fig. 9 A, ϕ_0 is 0 and therefore the bundle tilt $\alpha = (\phi - \phi_0) = \phi$. Fig. 9 *B* plots the loci of lateral displacement-orientation data pairs for all the target points along the undulating bundle. We vary all three parameters, i.e., the amplitude, the wavelength, and the phase shift of the sine function.

The theoretical loci do not represent lines, but ellipse-like curves (the curves have no closed form analytical representation). The deviations of the loci from a straight line correspond to the systematic error ε mentioned in the Discussion. However, the plot indicates that for a given shift δ_{retro} all the loci for different amplitudes and wavelengths form a multitude of concentric curves with a common axis whose slope is proportional to the shift, respectively speed of flow, and whose zero crossing is equal to ϕ_0. Therefore, independent of the type of undulation in the bundle, the measured data pairs $\{\delta_{lateral}, \phi\}$ lie symmetrically around the sought regression line.

APPENDIX B

Flow-field decomposition by least-squares collocation

Least-squares collocation (LSC) can be viewed as a general method of least-squares model fitting. It was first adopted in physical geodesy to propagate the gravity field through space (Moritz, 1980). Later it has been applied to tectonophysics for the analysis of complex displacement patterns in continental crust movements (Kahle et al., 1995). The main strength of the framework lies in the combination of functional and stochastic modeling of measurement data. This allows one to impose a relatively simple analytical description of the overall system behavior using low-order parametric functions. Neglected, yet significant high-order terms that cause mismatches between the real data and the simplified system description are picked up by a second stochastic term. Stochastic modeling requires much weaker knowledge of the system properties than analytical descriptions while still providing an accurate picture of the underlying system. Therefore, LSC is an ideal tool for modeling biological systems. Frequently, a biological system is too complex to be appropriately represented by a parametric formulation. Nevertheless, there is still a rough picture of the overall control mechanism available which can be formalized in a parametric function. The remaining parts of the complex behavior are represented by the stochastic term.

In the following we outline the concept of LSC for modeling the retrograde actin flow field. For any of the sampled target points we write the measured velocity vectors $\mathbf{v}(\mathbf{x})$ as

$$\mathbf{v}(\mathbf{x}) = \underbrace{\mathbf{t}^f(\mathbf{x}, \xi) + \mathbf{s}^f(\mathbf{x})}_{\mathbf{v}^f(\mathbf{x})} + \mathbf{e}(\mathbf{x}). \quad (7)$$

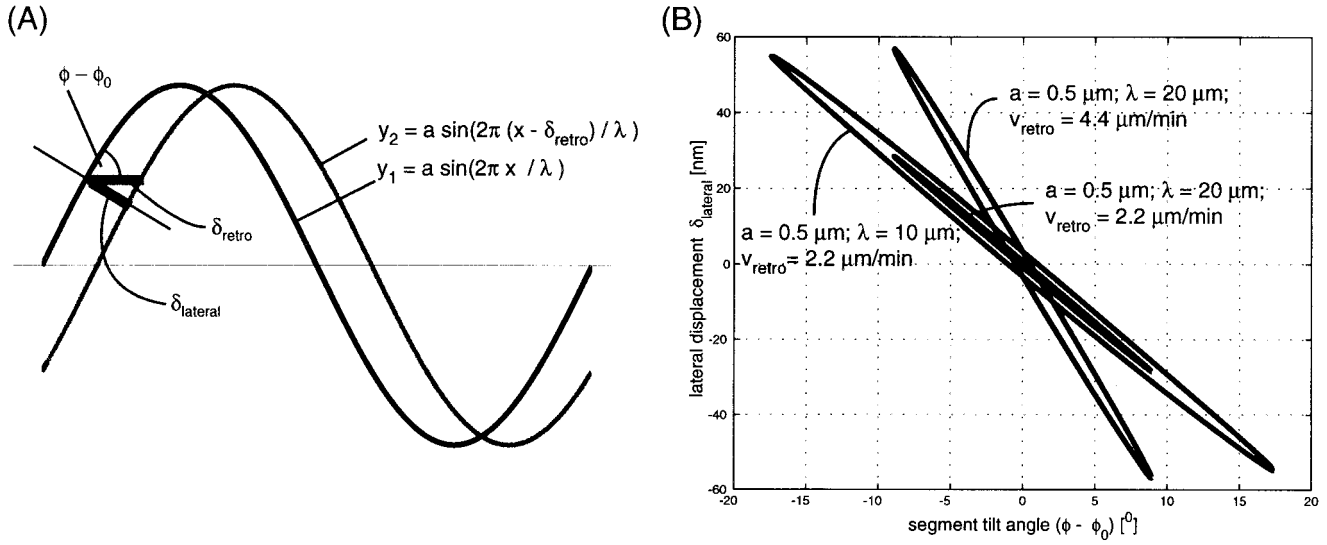

FIGURE 9 Simulation of the displacement-orientation data pairs for a moving bundle with sinusoidal shape. (*A*) A bundle is shown in two positions, which are displaced by δ_{retro} in x direction. The lateral displacement $\delta_{lateral}$ is constructed in accordance to the tracking procedure in Fig. 2, i.e., $\delta_{lateral}$ is determined by the distance between the target point and the intersection of the normal with the shifted bundle. (*B*) Theoretical loci of lateral displacement versus bundle tilt angle calculated for all target point positions along the bundle. The theoretical loci form an ellipse-like curve whose shape and orientation depends on the amplitude a and wavelength λ of the sinusoidal bundle and on the amount of the displacement δ_{retro}. The displacement is given as $\delta_{retro} = v_{retro}\,\Delta t$. Two such curves are calculated for values of a, λ, and v_{retro} that seem to be representative of the measurements shown in Fig. 4. The third curve is drawn for $v_{retro} = 4.4$ μm/min to demonstrate the change in the orientation of the ellipse when doubling the retrograde displacement.

The parametric term $\mathbf{t}^f(\mathbf{x}, \xi)$ describes the global flow as a function of the target point position $\mathbf{x}$ and the parameter vector ξ. The superimposed second term $\mathbf{s}^f(\mathbf{x})$ models a stochastic flow field with an expected zero mean vector. Further on, we refer to this term as the *flow signal* while the global term is called *flow trend.* The LSC model assumes that the signals $\mathbf{s}^f(\mathbf{x}^1)$ and $\mathbf{s}^f(\mathbf{x}^2)$ in two target points with coordinates $\mathbf{x}^1$ and $\mathbf{x}^2$ are correlated. The correlation decreases monotonically with increasing point-to-point distance. Therefore, the flow signal can pick up flow patterns that vanish in a global perspective, but which are significant flow events supported by matching velocities in several neighboring target points. The last term, $\mathbf{e}(\mathbf{x})$, accounts for random errors in the velocity measurements that are uncorrelated between the target points. The vector decomposition in Eq. 7 is depicted by Fig. 10. The unknown parameters of the trend as well as the signal and error vector in each target point are estimated subject to

$$\hat{\xi}, \hat{\mathbf{s}}^f(\mathbf{x}), \hat{\mathbf{e}}(\mathbf{x}) = \arg\min(\Sigma^T C_{ss} \Sigma + E^T C_{ee} E), \qquad (8)$$

where Σ and E are both column vectors concatenating the signal, respectively error vectors in all considered target points. The matrices C_{ss} and C_{ee} control the stochastic models for the signal and the error components of the flow field. C_{ss} describes the statistical correlation between the signal vectors in different target points. C_{ee} can be derived from the standard deviations of the velocity measurements obtained from regression analysis in each target point. Subtraction of the error vector $\mathbf{e}(\mathbf{x})$ from the original velocity measurement $\mathbf{v}(\mathbf{x})$ yields a new, filtered velocity vector $\mathbf{v}^f(\mathbf{x})$ that is consistent with the flow trend and the signals in all other target points of the field. With the same framework we can also interpolate velocity vectors at any location inside the lamellipodium. Analogously, interpolated velocity vectors $\mathbf{v}^i$ consist of a superposition of a global trend component and a signal vector (Fig. 10), thus

$$\mathbf{v}^i(\mathbf{x}) = \mathbf{t}^i(\mathbf{x}, \xi) + \mathbf{s}^i(\mathbf{x}). \qquad (9)$$

The solution to Eq. 8 will be described in a follow-up paper along with a further extension of LSC to the computation of strain rates generated by the various flow components.

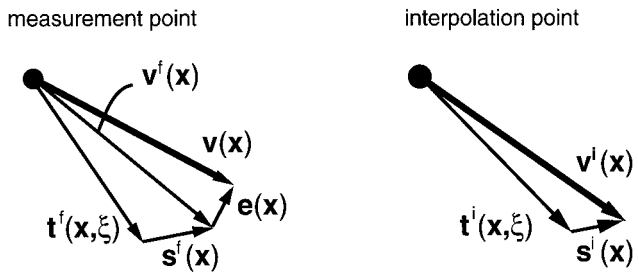

FIGURE 10 Flow field decomposition by least-squares collocation (LSC). In a target point the original measurement $\mathbf{v}(x)$ is divided into a parametric term $\mathbf{t}^f(\mathbf{x}, \xi)$, and two stochastic terms $\mathbf{s}^f(\mathbf{x})$ and $\mathbf{e}(\mathbf{x})$. The term $\mathbf{t}^f(\mathbf{x}, \xi)$ describes the global flow as a function of the target point position $\mathbf{x}$ and the parameter vector ξ. The superimposed term $\mathbf{s}^f(\mathbf{x})$ models a flow field with an expected zero mean vector. The LSC model assumes that the signals $\mathbf{s}^f(\mathbf{x}^1)$ and $\mathbf{s}^f(\mathbf{x}^2)$ in two target points with coordinates $\mathbf{x}^1$ and $\mathbf{x}^2$ are correlated. The correlation decreases monotonically with increasing point-to-point distance. Therefore, the signal can pick up flow patterns that vanish in a global perspective, but which are significant flow events supported by the correlating velocities in several neighboring target points. The term $\mathbf{e}(\mathbf{x})$ accounts for random errors in the velocity measurements which are supposedly uncorrelated between the target points. Subtraction of $\mathbf{e}(\mathbf{x})$ from the original measurement $\mathbf{v}(\mathbf{x})$ yields a new, filtered velocity vector $\mathbf{v}^f(\mathbf{x})$. In an interpolation point the velocity $\mathbf{v}^i(\mathbf{x})$ consists of a superposition of the global trend $\mathbf{t}^i(\mathbf{x}, \xi)$ and the spatially correlated signal $\mathbf{s}^i(\mathbf{x})$.

We are grateful to Raffael Burgy for programming LSC and for preparing the panels displayed in Fig. 8.

We acknowledge support from the Swiss National Science Foundation in form of a Young Investigator Award (to G.D.) and from the BioCurrent Research Center at the Marine Biological Laboratory, which is supported by the National Institutes of Health Grant P41RR-01385. This work was funded by the National Institutes of Health Grant GM 49210 (awarded to R.O.).

REFERENCES

Danuser, G., and M. Stricker. 1998. Parametric model fitting: from inlier characterization to outlier detection. *IEEE Trans. Pattern Analysis and Machine Intelligence*, 20:263–280.

Danuser, G., P. T. Tran, and E. D. Salmon. 2000. Tracking differential interference contrast diffraction line images with nanometre sensitivity. *J. Microsc.* 198:34–53.

Gelles, J., B. J. Schnapp, and M. P. Sheetz. 1988. Tracking kinesin-driven movements with nanometer-scale precision. *Nature*. 331:450–453.

Gittes, F., B. Mickey, J. Nettleton, and J. Howard. (1993). Flexural rigidity of microtubules and actin filaments measured from thermal fluctuations in shape. *J. Cell Biol.* 120:923–934.

Ishijima, A., T. Doi, K. Sakurada, and T. Yanagida, 1991. Sub-piconewton force fluctuations of actomyosin in vitro. *Nature*. 352:301–306.

Kahle, H.-G., M. V. Müller, A. Geiger, G. Danuser, S. Mueller, G. Veis, H. Billiris, and D. Paradissis. 1995. The strain field in northwestern Greece and the Ionian Islands: results inferred from GPS measurements. *Tectonophysics.* 249:41–52.

Katoh, K., K. Hammar, P. J. S. Smith, and R. Oldenbourg. 1999a. Arrangement of radial actin bundles in the growth cone of *Aplysia* bag cell neurons shows the immediate past history of filopodial behavior. *Proc. Natl. Acad. Sci. USA.* 96:7928–7931.

Katoh, K., K. Hammar, P. J. S. Smith, and R. Oldenbourg. 1999b. Birefringence imaging directly reveals architectural dynamics of filamentous actin in living growth cones. *Mol. Biol. Cell.* 10:197–210.

Lin, C. H., and P. Forscher. 1995. Growth cone advance is inversely proportional to retrograde f-actin flow. *Neuron.* 14:763–771.

Mogilner, A., and G. Oster. 1996. Cell motility driven by actin polymerization. *Biophys. J.* 71:3030–3045.

Moritz, H. 1980. Advanced Physical Geodesy. Wichmann, Karlsruhe, Germany.

Oldenbourg, R. 1996. A new view on polarization microscopy. *Nature.* 381:811–812.

Oldenbourg, R., K. Katoh, and G. Danuser. 2000. Mechanism of lateral movement of filopodia and radial actin bundles on neuronal growth cones. *Biophys. J.* 78:1176–1182.

Oldenbourg, R., and G. Mei. 1995. New polarized light microscope with precision universal compensator. *J. Microsc.* 180:140–147.

Oldenbourg, R., E. D. Salmon, and P. T. Tran. 1998. Birefringence of single and bundled microtubules. *Biophys. J.* 74:645–654.

Small, V., K. Rottner, P. Hahne, and K. I. Anderson. 1999. Visualising the actin cytoskeleton. *Microsc. Res. Tech.* 47:3–17.

Svoboda, K., C. F. Schmidt, B. J. Schnapp, and S. M. Block. 1993. Direct observation of kinesin stepping by optical trapping interferometry. *Nature.* 365:721–727.

Theriot, J. A., and T. J. Mitchison. 1991. Actin microfilament dynamics in locomoting cells. *Nature*. 352:126–131.

Wang, Y. L. 1985. Exchange of actin subunits at the leading edge of living fibroblasts: possible role of treadmilling. *J. Cell Biol.* 99:1478–1485.

Waterman-Storer, C. M., A. Desai, J. C. Bulinski, and E. D. Salmon. 1998. Fluorescent speckle microscopy, a method to visualize the dynamics of protein assemblies in living cells. *Curr. Biol.* 8:1227–1230.

Yin, H., R. Landick, and J. Gelles. 1994. Tethered particle motion method for studying transcript elongation by a single RNA polymerase molecule. *Biophys. J.* 67:2468–2478.